APPENDIX F:

Final Report - Nonlinear Wave Propagation in One and Two Dimensions

by

R.J. Archuleta and Kenichi Tsuda

Final Report
URS Group, Inc.
Subcontract No. DEN33258
Nonlinear Wave Propagation in One and Two Dimensions

Ralph J. Archuleta and Kenichi Tsuda
Institute for Crustal Studies, University of California, Santa Barbara

Introduction

We have applied the Bonilla (2000)'s and Iwan's (1967) method to calculate the site response at Jackson Lake Dam, Wyoming. This dam is located within 10 km from the Teton fault that is capable of causing a M_w 7 earthquake. Furthermore, this Dam is located above the sediment filled valley. A part of the Dam itself has a low shear-wave velocity layer (140 m/sec). Based on the geophysical data (O'Connell, 2002), we constructed a one-dimensional shear-wave velocity model for the dam. To examine the response of the dam we used records from earthquakes with both small and large amplitude as input motions at the base of the soil profile. The input motions are strong-motion records from the 1995 Mw=6.9 Kobe earthquake and the 1983 Mw=6.5 Coalinga earthquake. Another record from a moderate-sized earthquake is used to simulate weak motion. We also used synthetic ground motion from the scenario earthquakes (M_w 7.0) that could occur on the Teton fault.

Data

The Jackson Lake Dam is located at Jackson Lake, Wyoming. Figure 1 shows the seismicity in the Teton region for the 1950 through 1985. This region is located within the Intermountain seismic belt (Smith *et al.*, 1993a) that has caused large earthquakes such as the 1959 Hebgen Lake M_w 7.7 earthquake, and the 1983 Borah Peak M_w 7.3 earthquake. The Teton fault, within the outlined box in Figure 1, has the potential for large earthquakes with $M_w \geq$ 7.0.

The information of the soil column at the foundation of that Dam was provided by the United States Bureau of Reclamation (O'Connell, 2002). The surface geology near the dam (Figure 2) is mainly composed of the Quaternary sand (Smith *et al*, 1993b). The thickness of the

sediments above the basement is about 140 m. We constructed a one-dimensional velocity structure for the sediment layer based on the USBR information. Figure 3 shows the velocity depth profile. The dashed line corresponds to the depth at which the input motion is applied. The soil parameters of V_p, V_s, Q, and ρ (density) for each layer are listed in Table 1.

Table1: Soil parameters for each layer

Layer	Depth (m)	V_p (m/s)	V_s (m/s)	ρ (kg/m^3)	Q
1	0 – 2	1500	275	1750	20
2	2 - 10	1500	275	1750	20
3	10 - 27	1542	138	1750	20
4	27 - 43	1542	200	1800	50
5	43 - 65	1552	218	1850	50
6	65 - 77	1890	343	1850	50
7	77 - 104	2474	360	1900	50
8	104 - 106	2580	376	1900	50
9	106 - 108	2736	376	1900	50
10	108 - 116	2893	393	1950	50
11	116 - 140	3100	657	1950	50
Rock	140	3353	1006	2000	

In this study, two kinds of records are applied as input motion. The first group consists of data from previous earthquakes; the second group consists of synthetic ground motions from the scenario earthquakes. In the first group three records from different earthquakes are used. The Pleasant Valley Pumping Plant accelerogram was recorded during the 1983 Coalinga earthquake (M_w=6.5) and the other is the accelerogram recorded at the JMA Kobe station during the 1995 Kobe earthquake (M_w=6.9). A third record was taken from the Yokohama high-density strong motion array; it comes from a moderate size Central-Chiba earthquake (M_w=5.3). The station is located on thick sediments. The second group comes from scenario M_w 7.0 earthquakes that could occur on the Teton Fault. These synthetic motions were calculated by using 3-D Green's function method (O'Connell, 2002).

Method

We have used two methods to calculate the response of vertically propagating shear waves: Bonilla (2000) and Iwan (1967). In Bonilla's method the constitutive equations for the stress-strain relationship is based on the strain space multi-shear mechanism model proposed by Iai *et al* (1992). This model takes into account the pore pressure generation, modulus degradation, and cyclic mobility of the sands (*e.g*. Towhata and Ishihara, 1985). Hereafter we refer this this method as 'effective stress analysis'. We have also used Iwan's method that provides a different description of the nonlinearity. As shown later, both methods produce the same basic result.

The nonlinear soil behavior based on Iai's model is expressed in terms of five dilatancy parameters (Iai *et al*., 1992), basically determined by the laboratory test. Unfortunately, there is not enough information from the laboratory or in-situ field study data to check the validity of these soil parameters. We set the values of those dilatancy parameters based on generic data. We assumed that the sandy layer (10 m – 27 m), which has the smallest shear wave velocity (Table 1), is most likely to behave nonlinearly when subjected to large-amplitude ground motion. Figure 4 shows the liquefaction resistance curve, representing the strength of the sandy layer in terms of the parameters listed in Table 2.

Table 2: Dilatancy Parameters for the Sandy Layer (10 m – 27 m)

P1	P2	S1	W1	C1
0.45	0.70	0.01	3.3	1.2

Before propagating the ground motion from 140 m depth, each of the recorded motions were modified to approximate the input motion at 140 m. Using the Thompson-Haskell method the Coalinga record was deconvolved to 140 m using the velocity profile in Table 1. For all other input motions, *i.e*. Kobe, Central-Chiba, and scenario earthquakes, we multiplied each by 0.5 to remove the effect of the free surface. The synthetic input motions were low-pass filtered below 8 Hz, the maximum frequency in the synthetic computation. All output time series are bandpass filtered 0.05 to 10 Hz.

Results

Coalinga Earthquake

Figure 5 shows the depth distribution of the maximum values of strain, pore pressure, mean stress, and shear stress when the 1983 Coalinga record, peak velocity 0.14 m/s, is used as input motion. In the sandy layer, corresponding to 10 to 27m depths, large strain and pore pressure buildup can be seen. The maximum strain is about 5% with the obvious interpretation that this section of the soil is responding nonlinearly.The calculated velocity time histories (left) at the surface (0m), 10m, 20m, 30m, 50m, 100m depth and their corresponding velocity response spectra (right) are shown in Figure 6. Below the sandy layer, the peak velocities are amplified; while above the sandy layer (0m, 10m, 20m depths), the peak velocities are attenuated. The response spectra show a shift of the fundamental frequencies to the longer period.

Kobe Earthquake

Figure 7 shows the depth distribution of the maximum values of strain, pore pressure, mean stress, and shear stress when using the record for the 1995 Kobe earthquake, peak velocity 0.41□m/s as the input motion. The strain profile is very similar in shape to that found for the Coalinga earthquake. The calculated time histories and response velocity spectra are plotted in Figure 8 at the same depths—0m, 10m, 20m, 30m, 50m, 100m—shown in Figure 6. As seen for the Coalinga input motion, there is deamplification of peak velocity for depths less than 27 m and a shift of fundamental frequencies to the longer period in the response spectra.

Central-Chiba Earthquake

To examine the soil behavior for a moderate-sized event we used a M 5.3 earthquake as input motion, maximum peak velocity of 0.018 m/s. Figure 9 shows the depth distribution of the maximum values of strain, pore pressure, mean stress, and shear stress. Compared to the Coalinga and Kobe case, not only is maximum strain much less than 1%, but also there is no pore pressure buildup for the sandy layer. The response spectra at the different levels are nearly the same with no shift in the fundamental frequencies (Figure 10). All of this indicates that the soil response is linear for this level of input.

Scenario Earthquake

We have used two components of motion from a scenario M_w 7 earthquake. In Figures 11 and 13 we show the depth distribution of maximum values of strain, pore pressure, mean stress, and shear stress for the EW component and NS components, respectively. The shape of the depth distributions of the maximum strain are similar to that found for Kobe and Coalinga

records. However the values of maximum strain are much larger. For both the EW and NS components, the maximum strains exceed 15%. Maximum strain over 10 % is very rare; this generally indicates that a soil may already have liquefied during the shaking (Ishihara, 1996). Some cases with maximum strain over 15% have been reported in laboratory tests of soils from the Kobe area (Ishihara, *et al.* 1998).

Figures 12 and 14 show the calculated velocity time histories and corresponding velocity response spectrum at the same depths as the other cases. The characteristics of the peak velocity and response spectra are similar to that found using recorded accelerograms: deamplification of the maximum velocity and a shift of fundamental period.

Total Stress Analysis and Comparisons with Iwan's Model

Porepressure buildup and the functional form of the nonlinear constitutive equation are two important factors when performing nonlinear analysis (Kramer, 1996). The pore pressure buildup causes the reduction of the soil strength; the nonlinear stress-strain constitutive equation specify the shape of hysteresis loop, material damping. To examine these effects we use as input the EW and NS ground motions from the scenario earthquake.

To examine the effect of the pore pressure we computed the ground motion for the total stress analysis, that is, no pore pressure is generated. Figure 15 shows the results of the comparison for the distribution of the maximum strain between the effective and the total stress analysis. The maximum strains from the total stress analysis are smaller than those from the effective stress analysis. However, the maximum strains below the sandy layer are very similar. Figures 16 and 17 show the time histories of acceleration, shear stress, and shear strain at a depth of 20 m, a point within the sandy layer. It is clear that the strain is much larger for the effective stress analysis as would be expected if the pore pressure increases and simultaneously decreases the mean stress.

To check on the results for a different nonlinear model of soil response, we used the constitutive equation for Iwan's (1967) model. Figure 17 shows the comparison of the depth distribution of maximum strain between the Iai model and the Iwan model. The maximum strain distribution from the Iwan model is basically similar to that determined by the Iai model, but the Iwan model does produce larger strains in the sandy layer 10-27 m. In Figures 19 and 20 we show the shear stress and pore pressure time histories as well as the phase diagrams for shear stress versus strain and shear stress versus mean stress. All of the results in these two figures are

for a depth of 20 m. Compared to Iai's model, the Iwan model produces smaller peak values of shear stress, less variation in the pore pressure and more confined phase diagram of stress versus strain. These features reflect the fact that hysteresis damping for Iwan model can be controlled. Nonetheless, the Iwan model does produce a larger peak strain. Overall, the basic conclusion is that Iai's model and Iwan's model produce very similar results. Both predict very large strains in the sandy layer and 100% pore pressure buildup when the input ground motion is large.

Conclusions and Future Study

The analysis of nonlinear seismic wave propagation was applied to the soil column at the Jackson Lake Dam. The analysis included using data from three recorded earthquakes and one scenario earthquake. If the input motion has large particle velocities, such as those from the earthquakes with $M_w \geq 6.5$, the low-velocity sand layer (10 – 27 m depth) produced strains of 5-20% and 100% pore pressure buildup. This behavior was not observed for the one small earthquake recording with a peak velocity of 0.018 m/s. In comparing two different formulations of the nonlinear constitutive equation by Iai and Iwan, we found similar results for the sand layer—maximum strains exceeding 10% and as large as 20% at some depths.

These results are based on one-dimensional wave propagation. Given the geometry of the dam and the variability in soil properties along the axis of the dam or in cross-section it may be necessary to consider two-dimensional nonlinear wave propagation for a more accurate prediction of the response under strong shaking.

References

Aguirre, J. and K. Irikura. (1997). Nonlinearity, liquefaction, and velocity variation of soft soil layers in Port Island, Kobe, during the Hyogo-ken Nanbu earthquakes, *Bull. Seismol. Soc. Am.,* ***87***, 1244 – 1258.

Beresnev, I. A. and K. L. Wen. (1996). Nonlinear site response – A reality?, *Bull.Seismol. Soc. Am.,* ***86****,* 1964 – 1978.

Bonilla, L. F. (2000). Computation of linear and nonlinear site response for near field ground motion*, Ph.D Thesis*, University of California, Santa Barbara, 285pp.

Field, E. H. and K. H. Jacob. (1995). A comparison and test of various site response techniques, including three that are not reference site dependent (1995). *Bull. Seismol. Soc. Am.,* ***85****,* 1127 – 1143, 1995.

Field, E. H., P. A. Johnson, I. A. Beresnev, and Y. Zeng (1997). Nonlinear ground-motion amplification by sediments during the 1994 Northridge earthquake, *Nature,* ***390***, 599 – 602.

Iai, S.,Y. Matsunaga, and T. Kameoka (1992). Strain space plasticity model for cyclic mobility, *Soils and Foundations,* ***32***, 1 – 15.

Ishihara, K., M. Cubrinovski, and T. Nonaka. (1998). Characterization of undrained behavior of soils in the reclaimed area of Kobe*, Soils and Foundations, Special Issues on Geotechnical Aspects of the January 17, 1995 Hyogoken-Nanbu Earthquakes* ***Vol 2***, 33-46.

Ishihara, K. (1996). Soil Behaviour in Earthquake Geotechnics, Clareton Press, Oxford, 350pp.

Iwan, W. D. (1967). On a class of models for the yielding behavior of continuous and composite systems, *J. Appl. Mech.* ***34***, 612 – 617.

Kramer, S. L. (1996) Geotechnical Earthquake Engineering, Prentice-Hall, NJ, 653pp.

O'Connell, D.R.H. (2002). Personal (written) communications.

Smith, B. R., Pierce, K. D., and Wold, J. R. (1993a). Seismic surveys and Quaternary history of Jackson Lake, Wyoming, in Snoke, A. W., Steidmann, J. R., and Roberts, S. M., editors, *Geology of Wyoming: Geological Survey of Wyoming Memoir No. 5*, p. 668-693.

Smith, B. R., Byrd, J. O, D., and Sunsong, D.D. (1993b). The Teton fault, Wyoming: seismotectonics, Quaternary history, and earthquake hazards, in Snoke, A. W., Steidmann, J. R., and Roberts, S. M., editors, *Geology of Wyoming: Geological Survey of Wyoming Memoir No. 5*, p. 628-667

Towhata, I., and K. Ishihara. (1985). Modeling soil behavior under principal axes rotation, *Fifth International Conference on Numerical methods in Geomechanics*, Nagoya, 523 – 530.

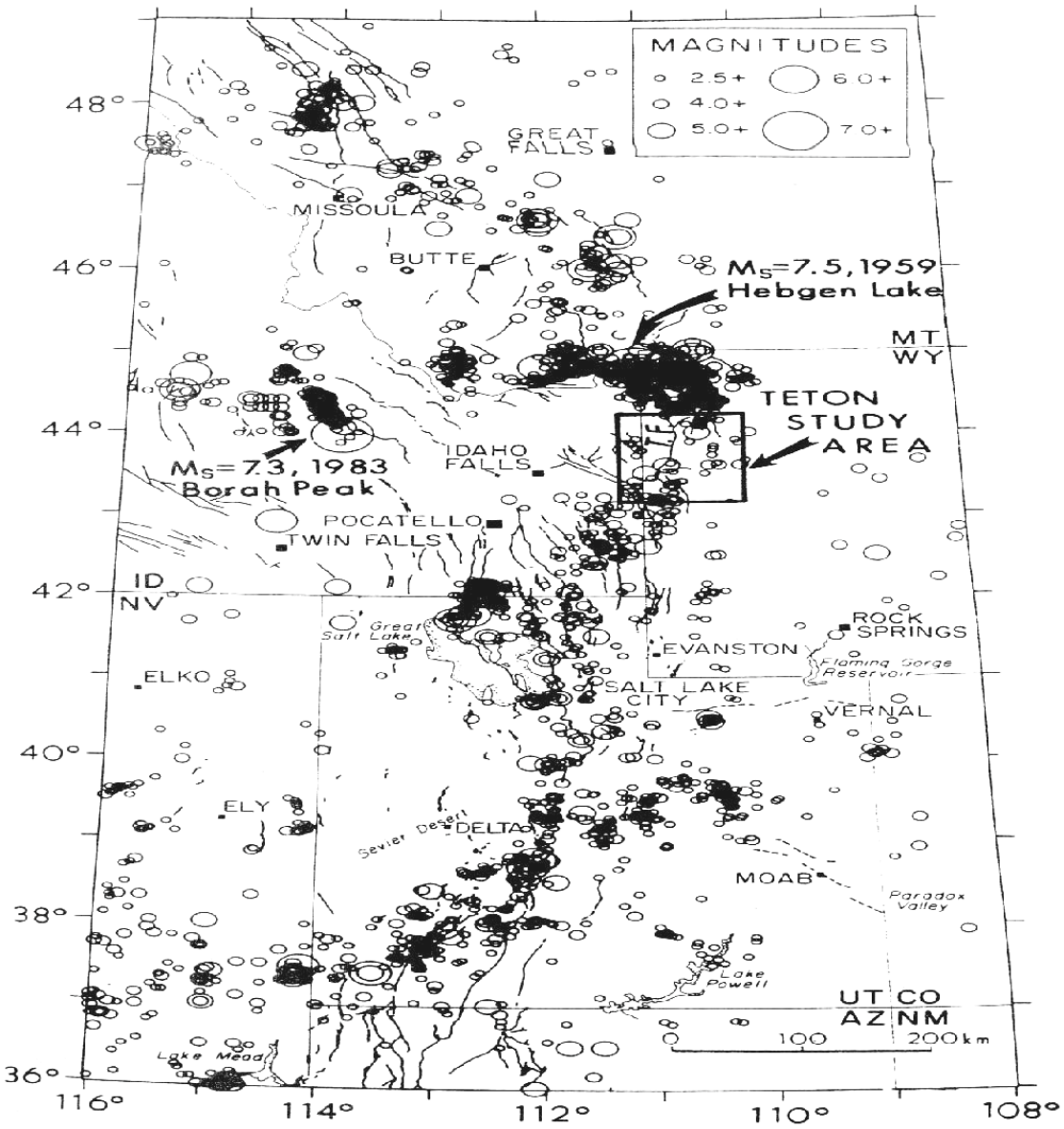

Figure 1: The seismicity of the intermountain seismic belt which is the general tectonic setting for the Jackson Lake Dam. Each circle corresponds to the size of earthquakes. The radius of each circle corresponds to the magnitude of each event. (Smith, *et al.*, 1992a)

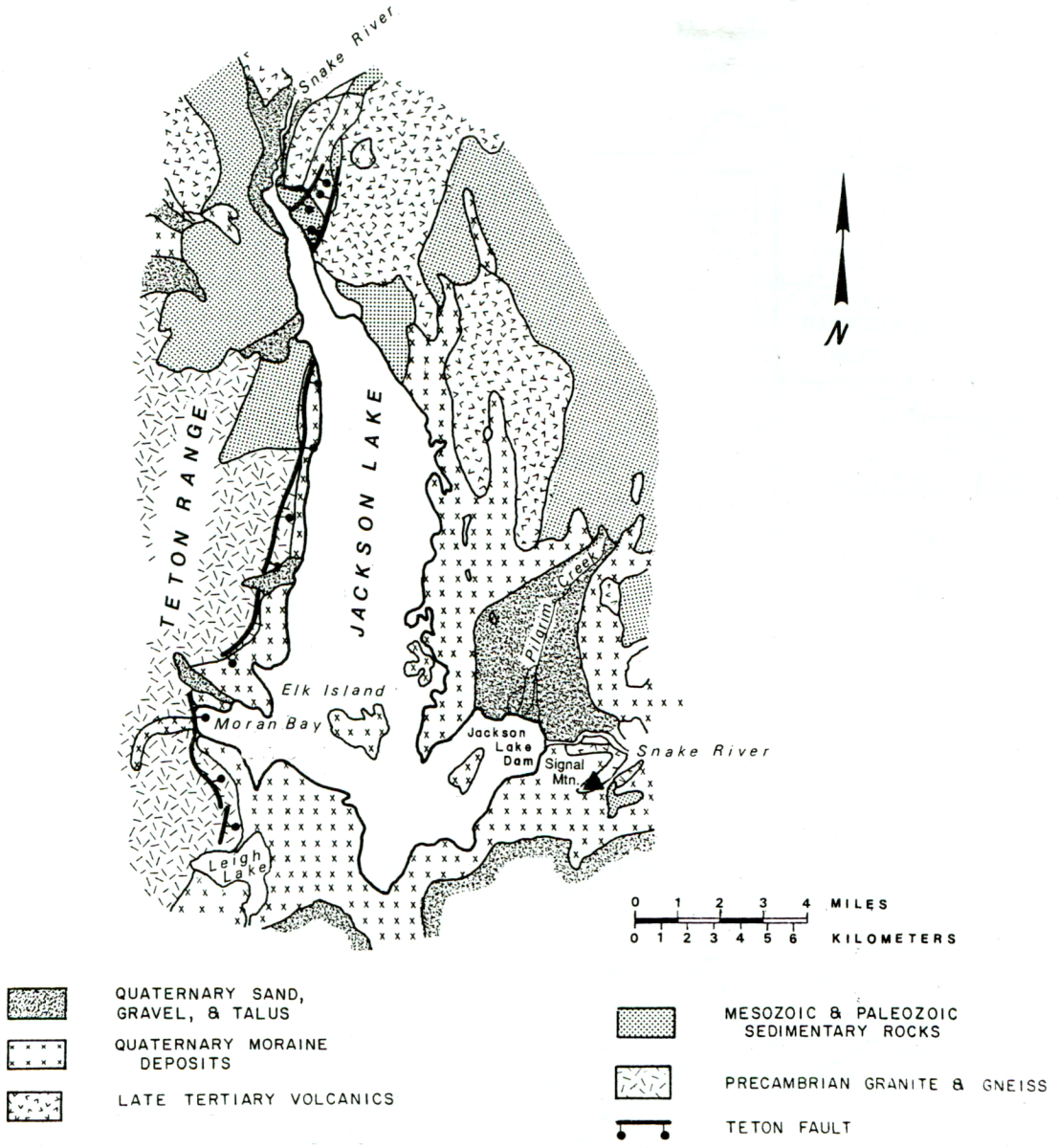

Figure 2: Surface geology around Jackson Lake Dam. (Smith *et al.*, 1992b)

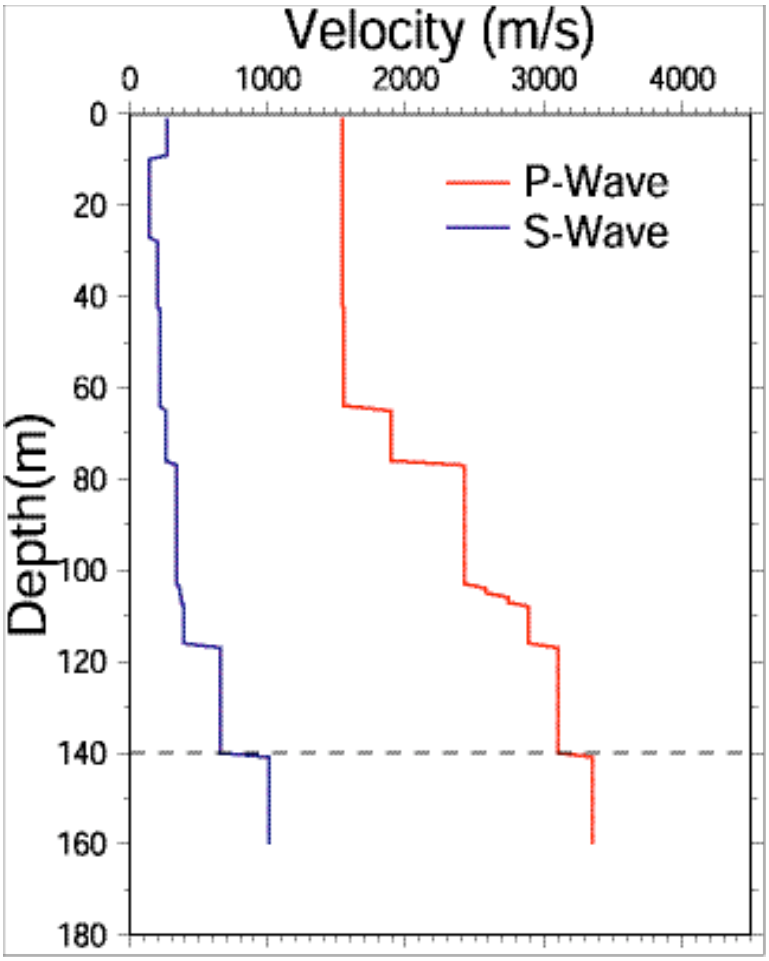

Figure 3: One-dimensional velocity structure for the Jackson Lake Dam. The dashed line corresponds to the depth at which input motion are introduced.

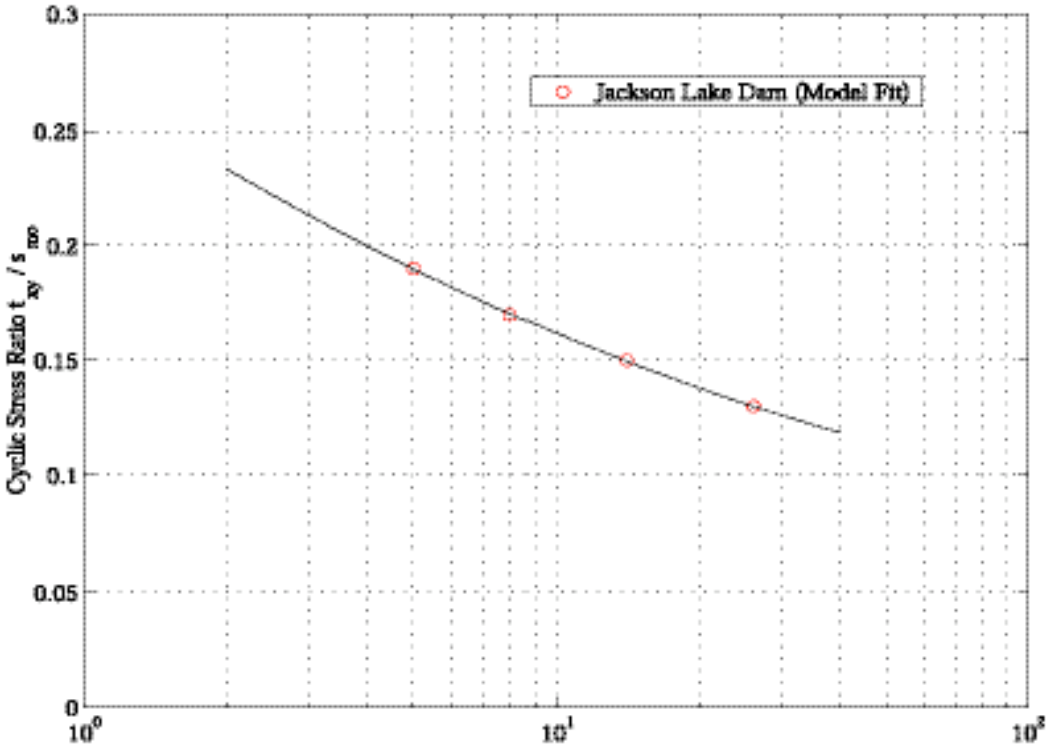

Figure 4: Liquefaction resistance curve for the materials of the sand layer (10–27 m depth) based on the five dilatancy parameters (Iai *et al.*, 1992) that control the nonlinear soil behavior. Parameters (Table 2) are taken from generic data for sand.

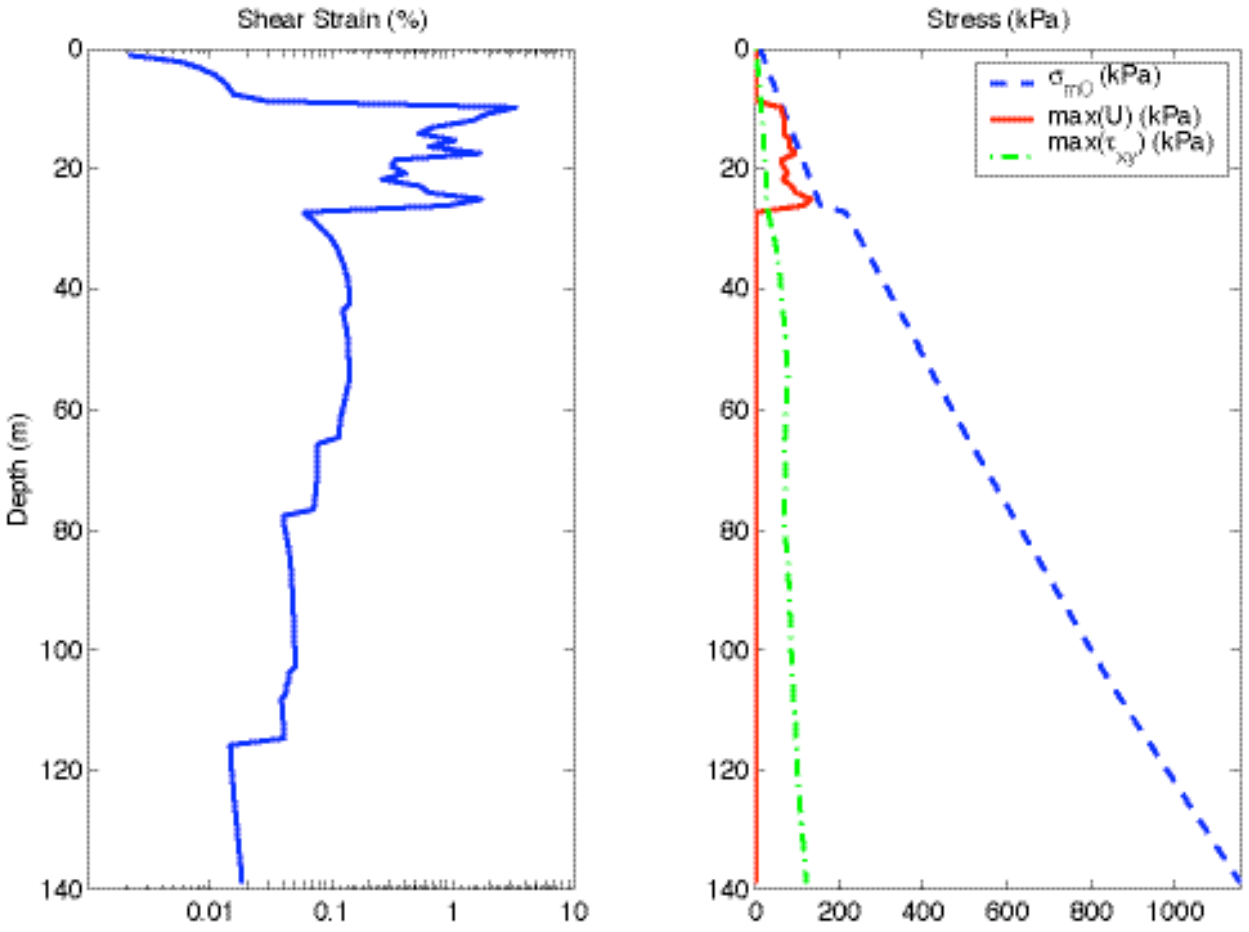

Figure 5: The depth distribution of the maximum strain, mean stress σ_{mo}, pore pressure U, and shear stress τ_{xy}, computed using the deconvolved Coalinga record as input at 140 m.

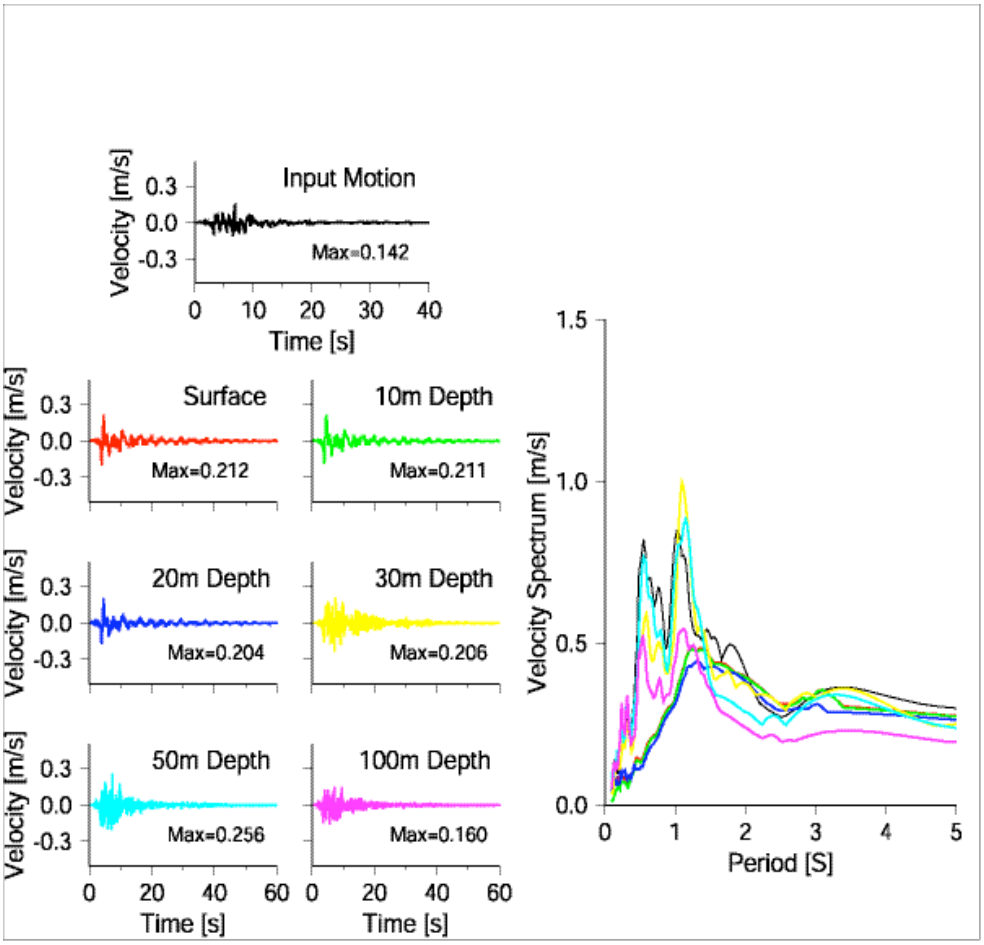

Figure 6: Calculated velocity time histories at 0m, 10m, 20m, 30m, 50m, and 100m depths and corresponding velocity response spectrum when using the deconvolved Coalinga record as the input at 140 m. The response spectra are color matched to the velocity time histories at different depths.

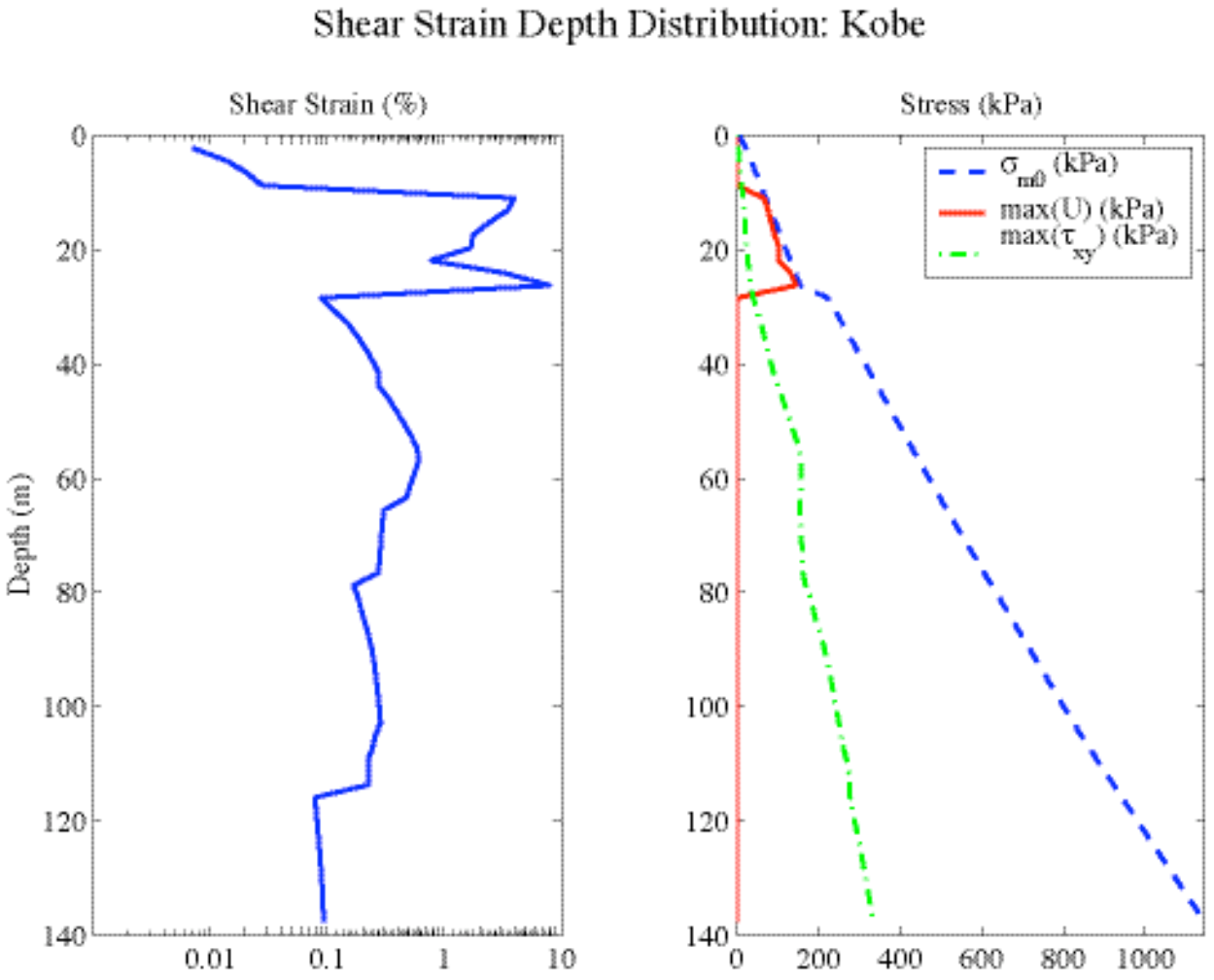

Figure 7: The depth distribution of the maximum strain, mean stress σ_{mo}, pore pressure U, and shear stress τ_{xy}, computed using the Kobe earthquake record as input at 140 m.

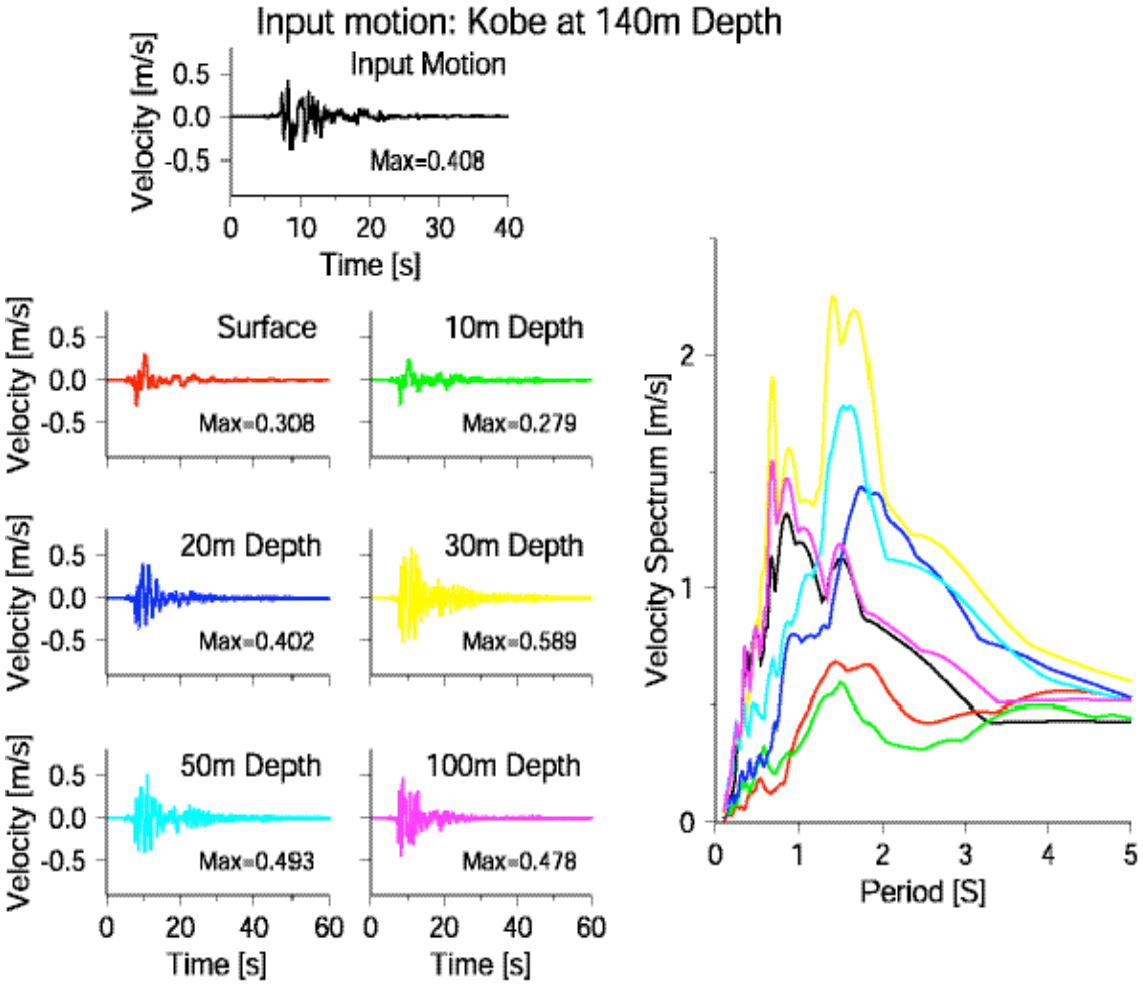

Figure 8: Calculated velocity time histories at 0m, 10m, 20m, 30m, 50m, and 100m depths and corresponding velocity response spectrum when using the record from the Kobe earthquake as input at 140 m. The response spectra are color matched to the velocity time histories at different depths.

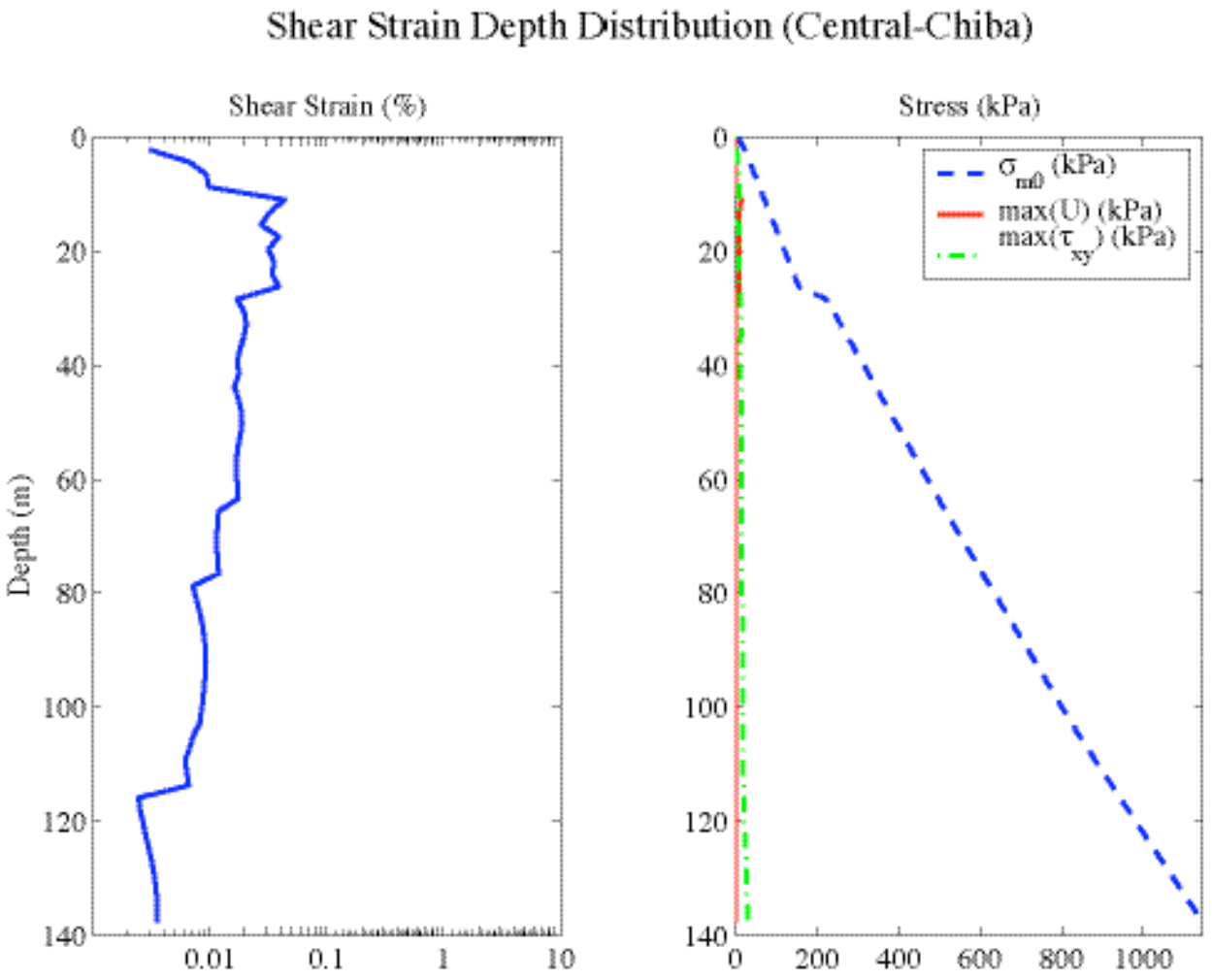

Figure 9: The depth distribution of the maximum strain, mean stress σ_{mo}, pore pressure U, and shear stress τ_{xy}, computed using Central-Chiba earthquake record as input at 140 m.

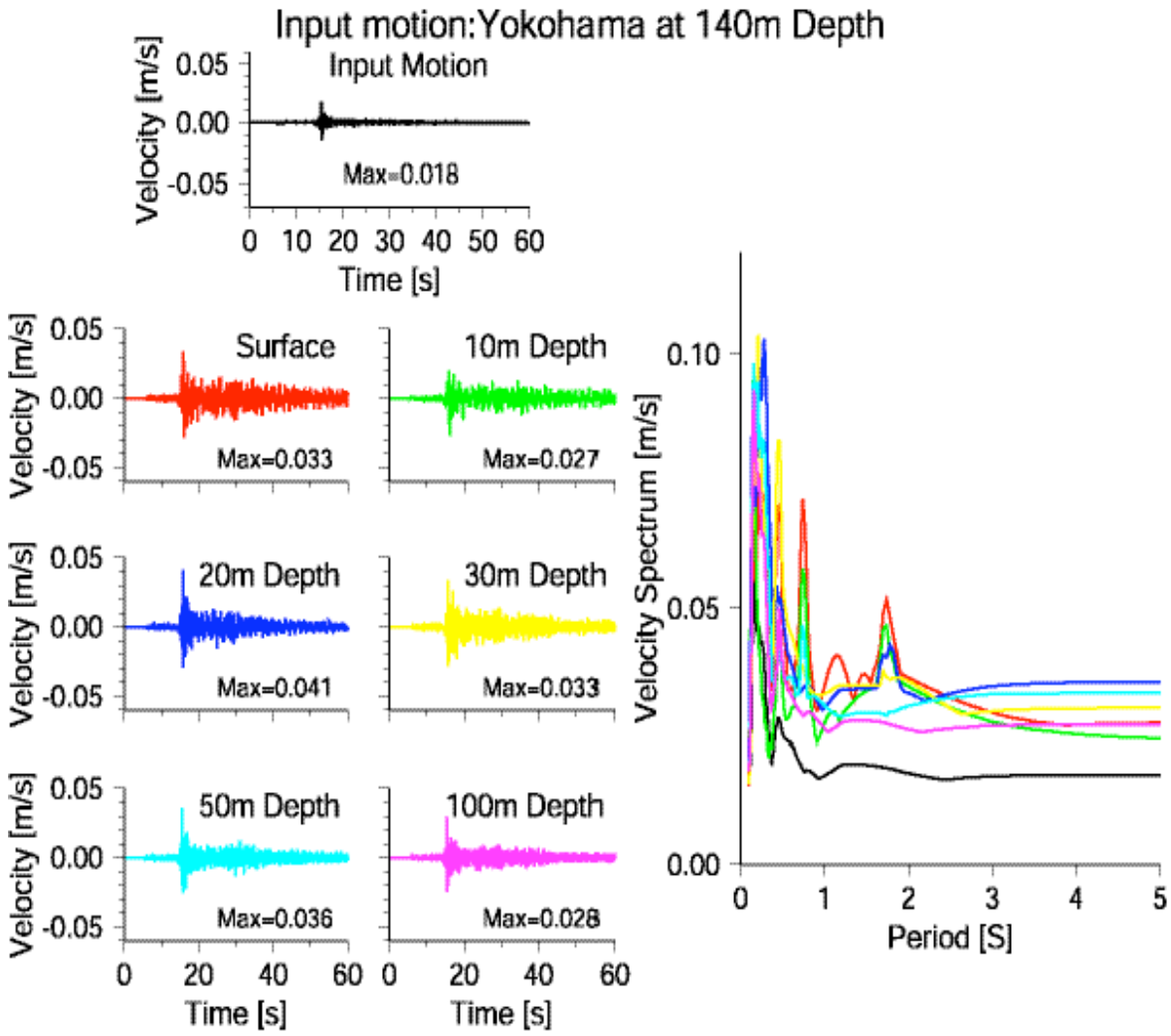

Figure 10: Calculated velocity time histories at 0m, 10m, 20m, 30m, 50m, and 100m depths and corresponding velocity response spectrum when using the record from Central-Chiba earthquake as input at 140 m. The response spectra are color matched to the velocity time histories at different depths.

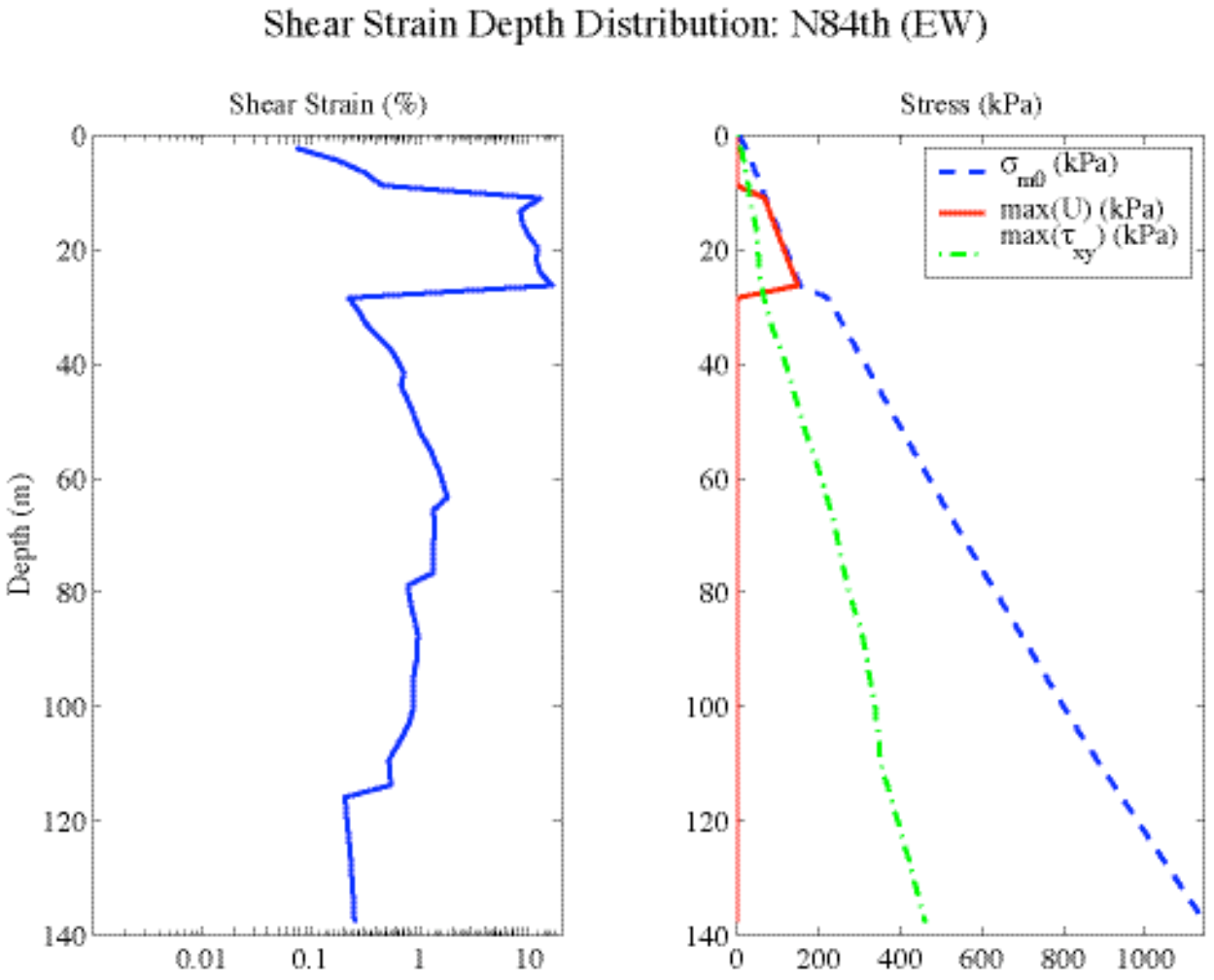

Figure 11: The depth distribution of the maximum strain, mean stress σ_{mo}, pore pressure U, and shear stress σ_{xy}, computed using the synthetic motion from the scenario earthquake (EW component) is used as input at 140 m.

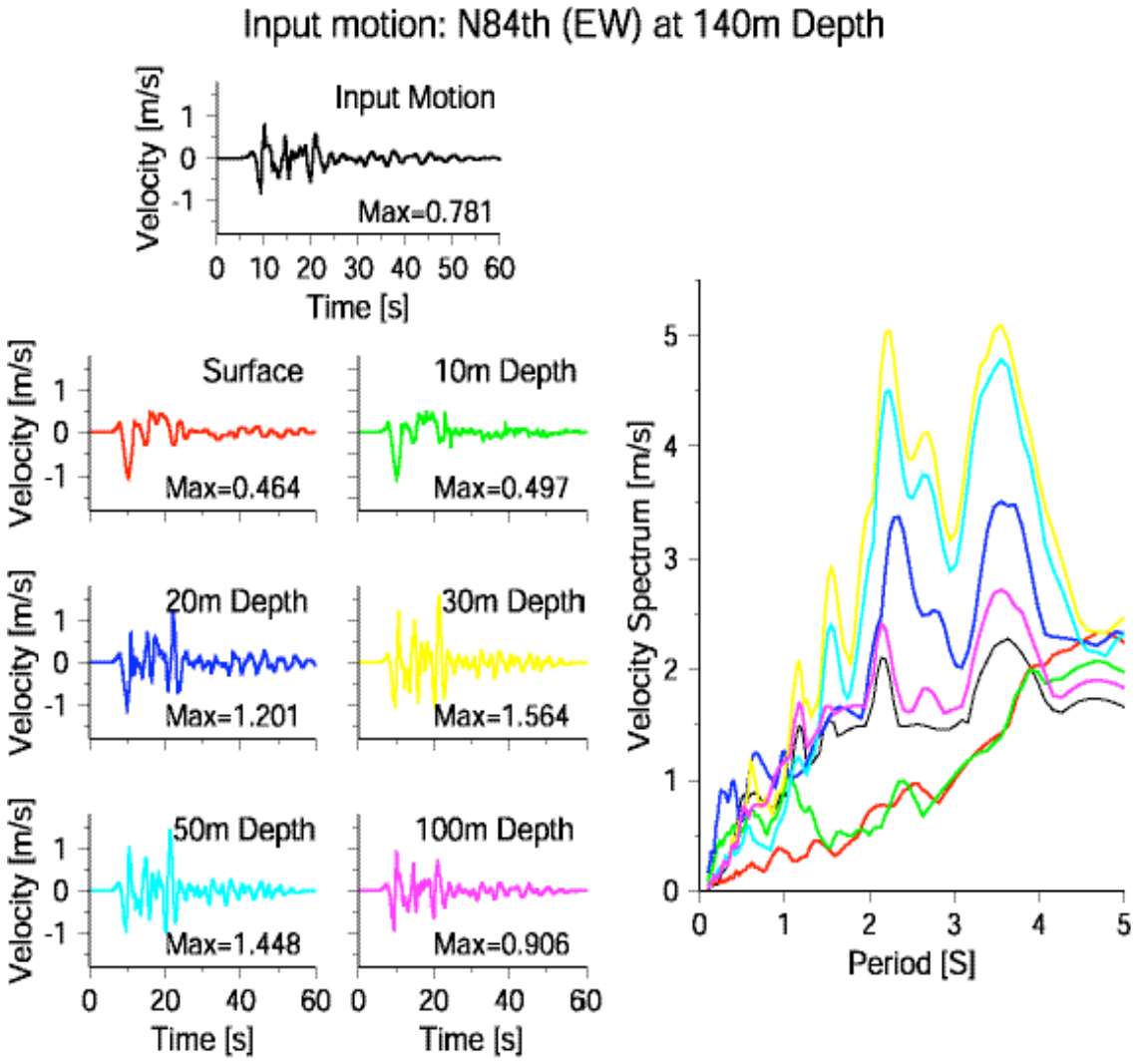

Figure 12: Calculated velocity time histories at 0m, 10m, 20m, 30m, 50m, and 100m depths and corresponding velocity response spectrum when the synthetic motion from the scenario earthquake (EW component) is used as input at 140 m.

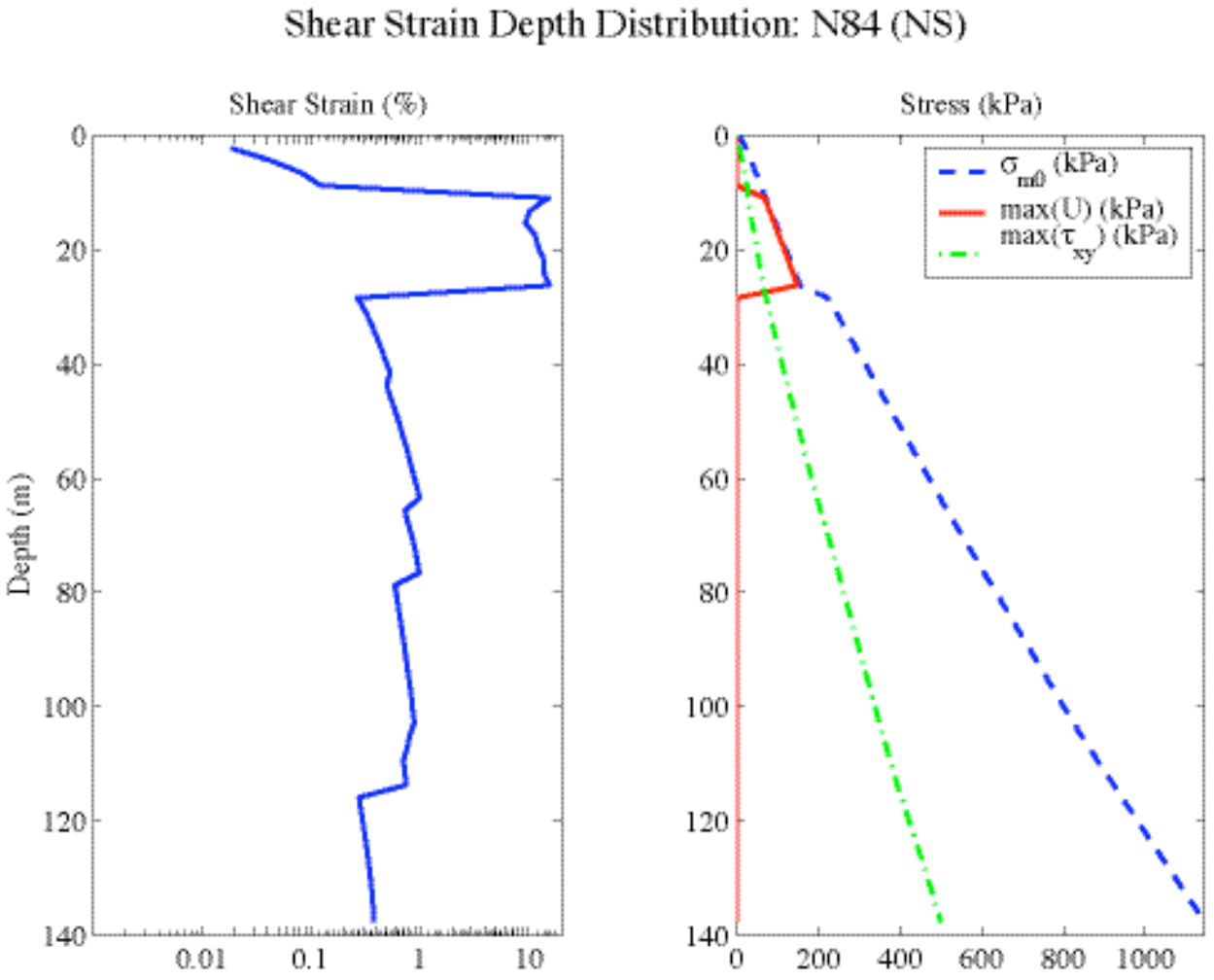

Figure 13: The depth distribution of the maximum strain, mean stress σ_{mo}, pore pressure U, and shear stress σ_{xy}, computed using the synthetic motion from the scenario earthquake (NS component) is used as input at 140 m.

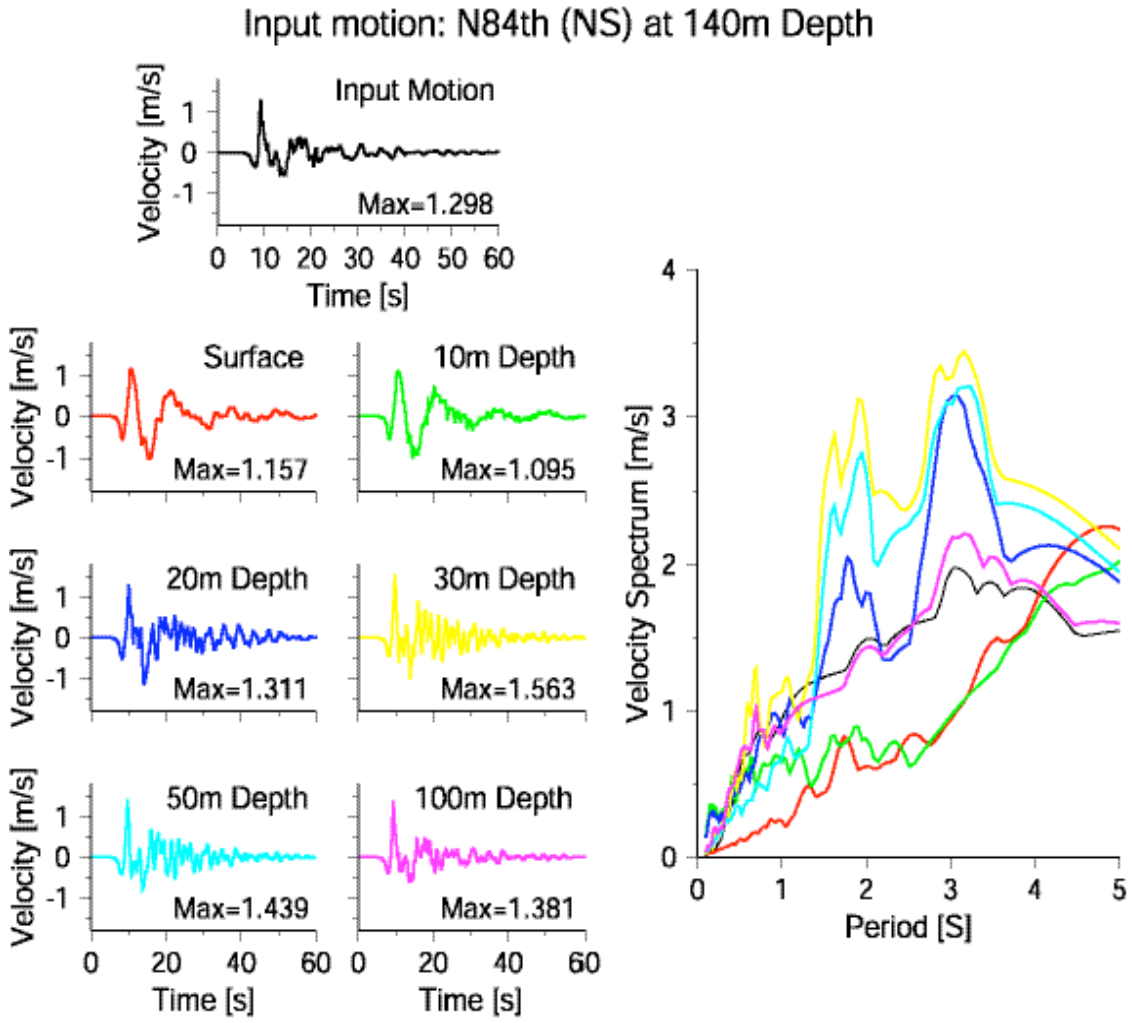

Figure 14: Calculated velocity time histories at 0m, 10m, 20m, 30m, 50m, and 100m depths and corresponding velocity response spectrum when the synthetic motion from the scenario earthquake (NS component) is used as input at 140 m.

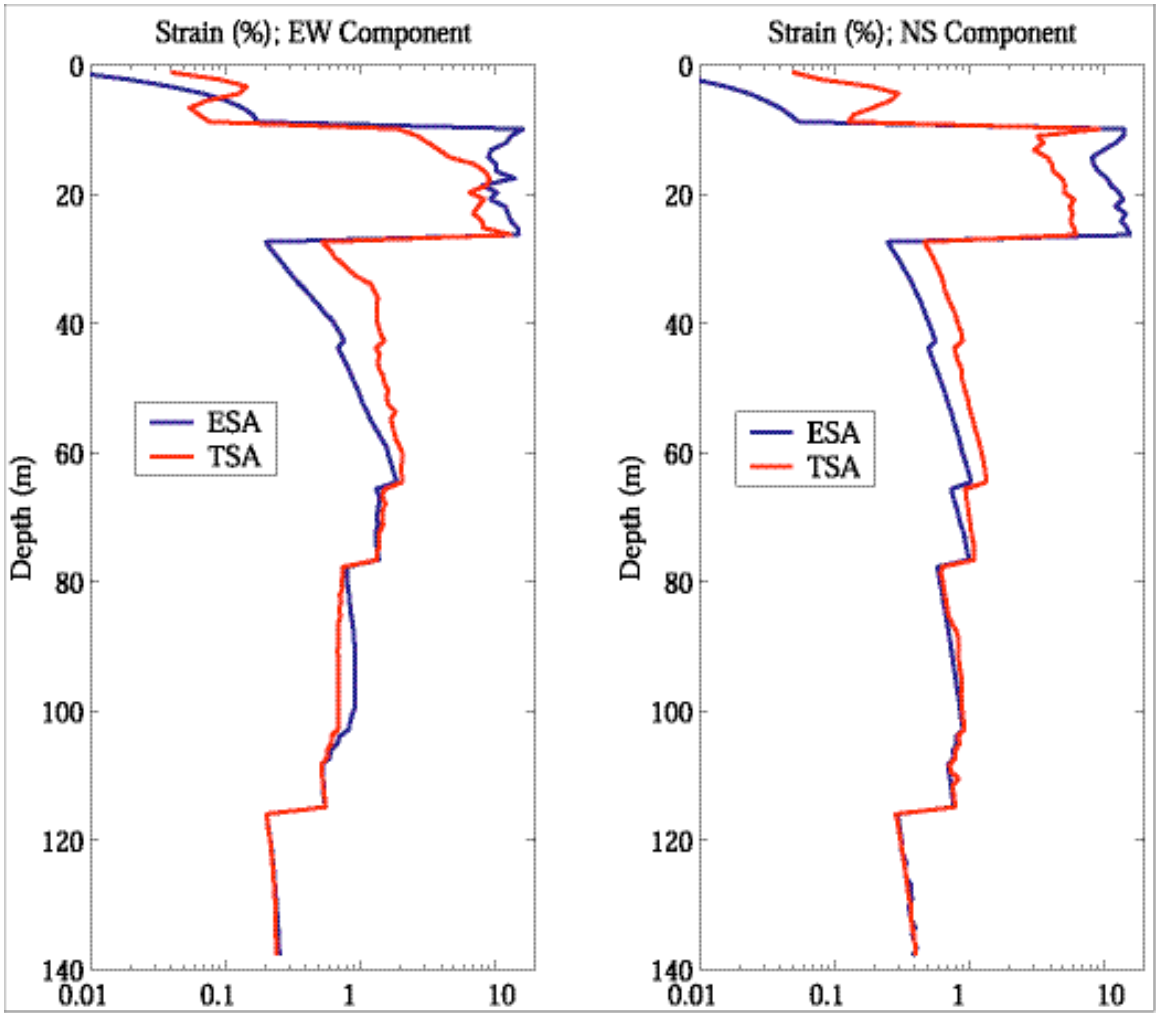

Figure 15: A comparison of distribution of the maximum strain with depth between effective stress analysis (ESA: blue lines) and total stress analysis (TSA: red lines) for EW and NS component of synthetic motions from the scenario earthquakes.

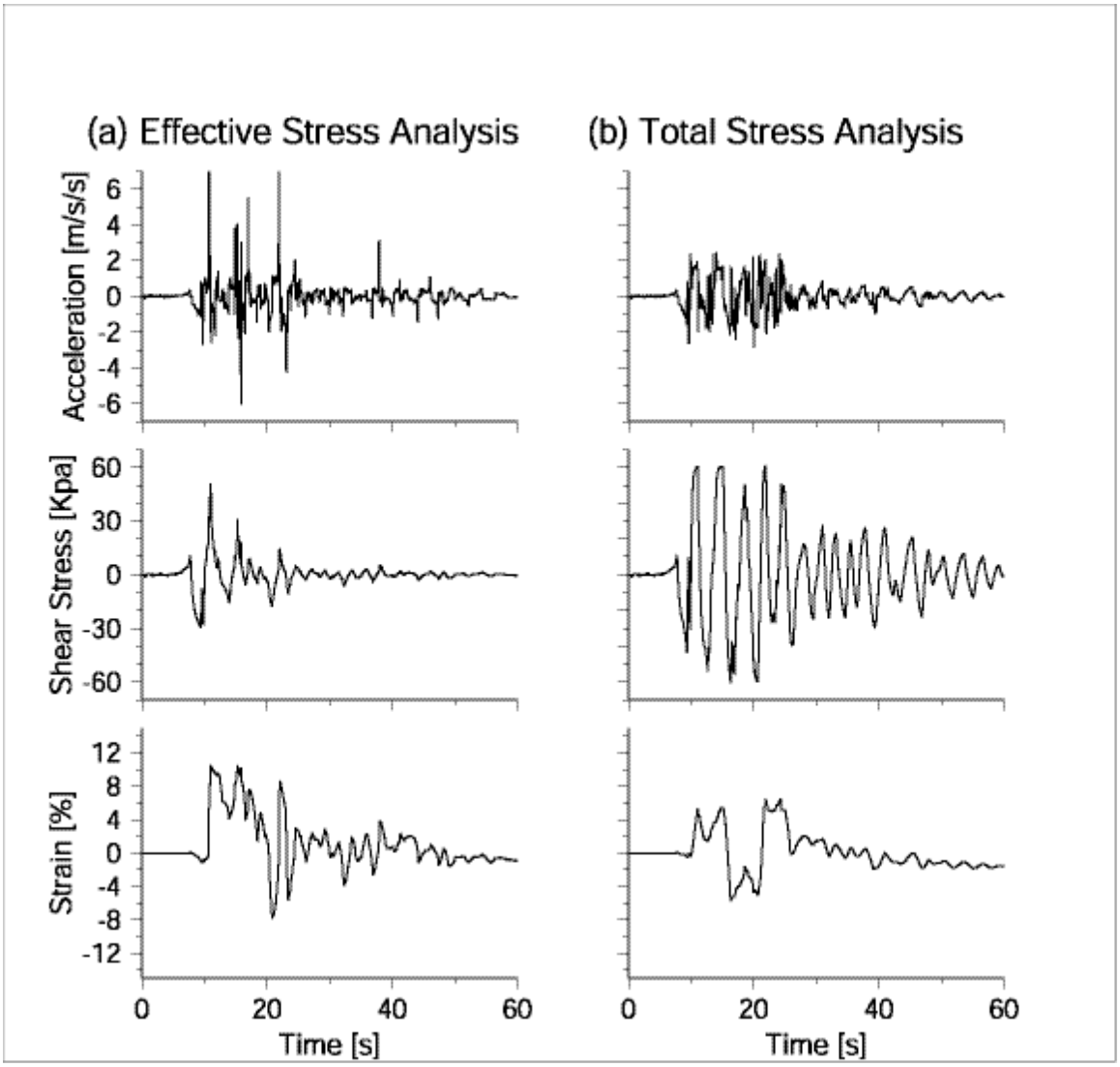

Figure 16: Calculated time histories of acceleration, shear stress, and strain at 20m depth (within the sand layer 10-27 m) from the effective stress analysis (a) and from the total stress analysis (b). The EW synthetic motion from the scenario earthquake is used as input.

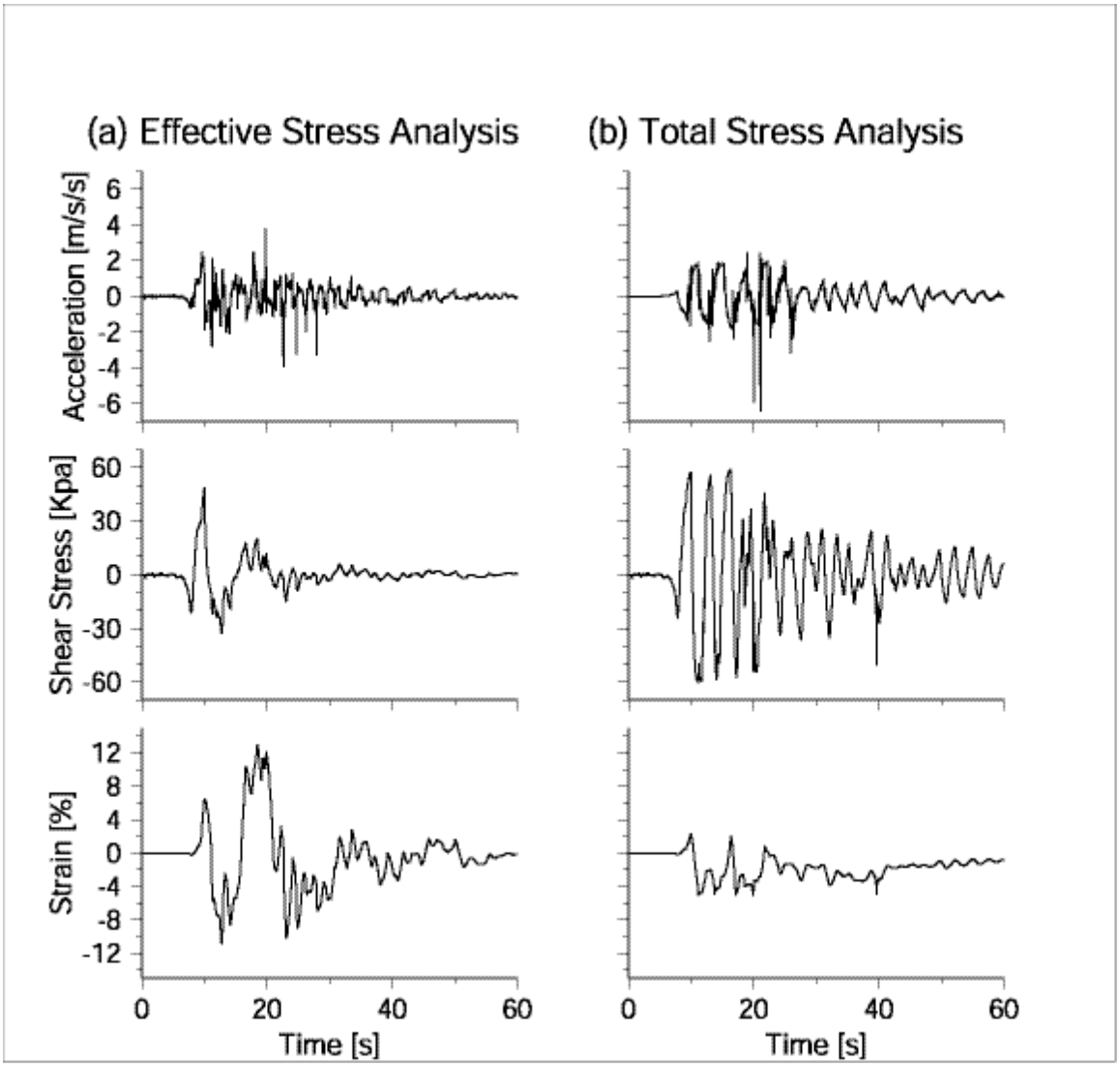

Figure 17: Calculated time histories of acceleration, shear stress, and strain at 20m depth (within the sand layer 10-27 m) from the effective stress analysis (a) and from the total stress analysis (b). The NS synthetic motion from the scenario earthquake is used as input.

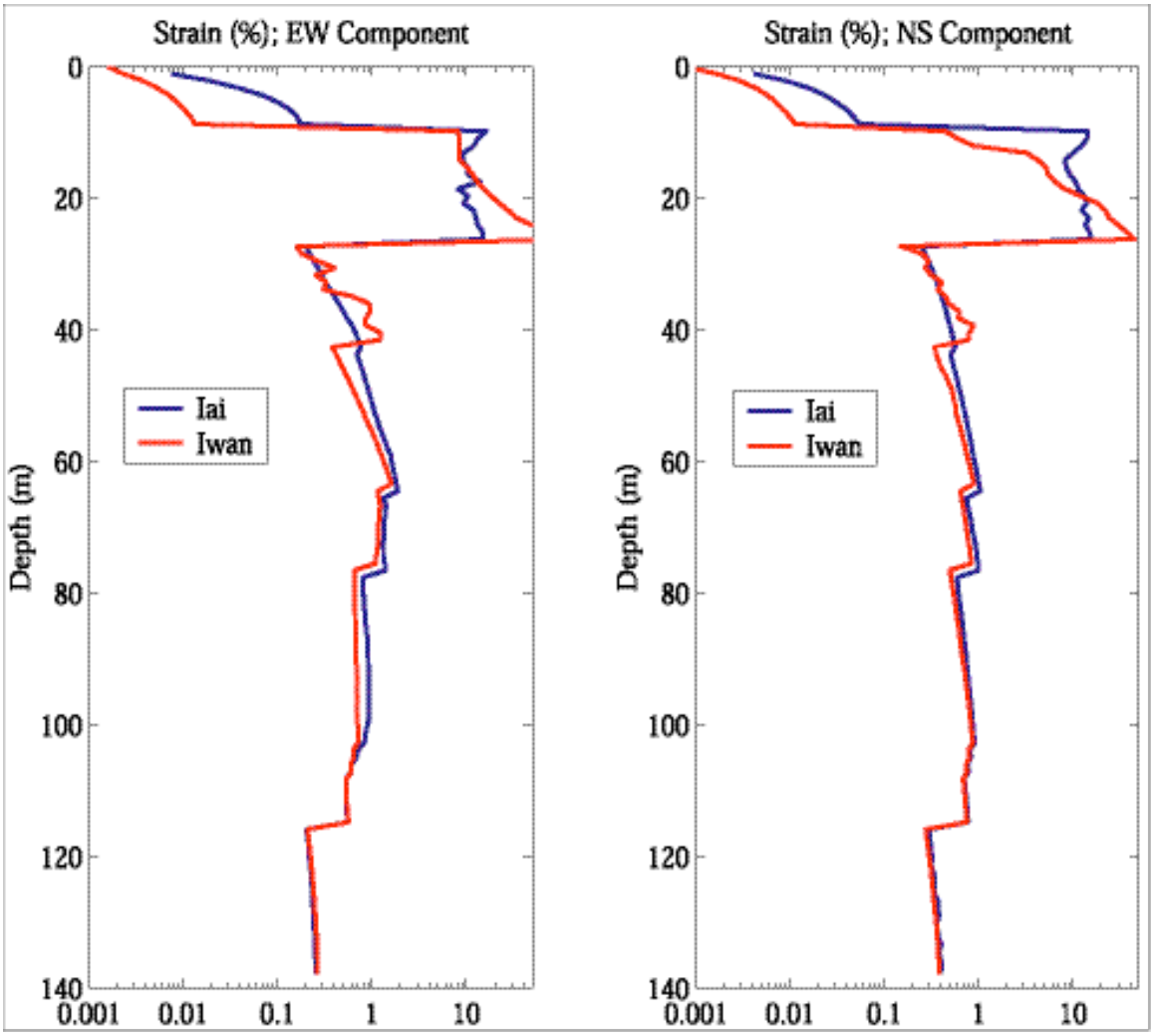

Figure 18: Comparison of the depth distribution of the maximum strain computed using the Iai model (blue lines) and the Iwan model (red lines) for EW and NS component of ground motion from the scenario earthquake.

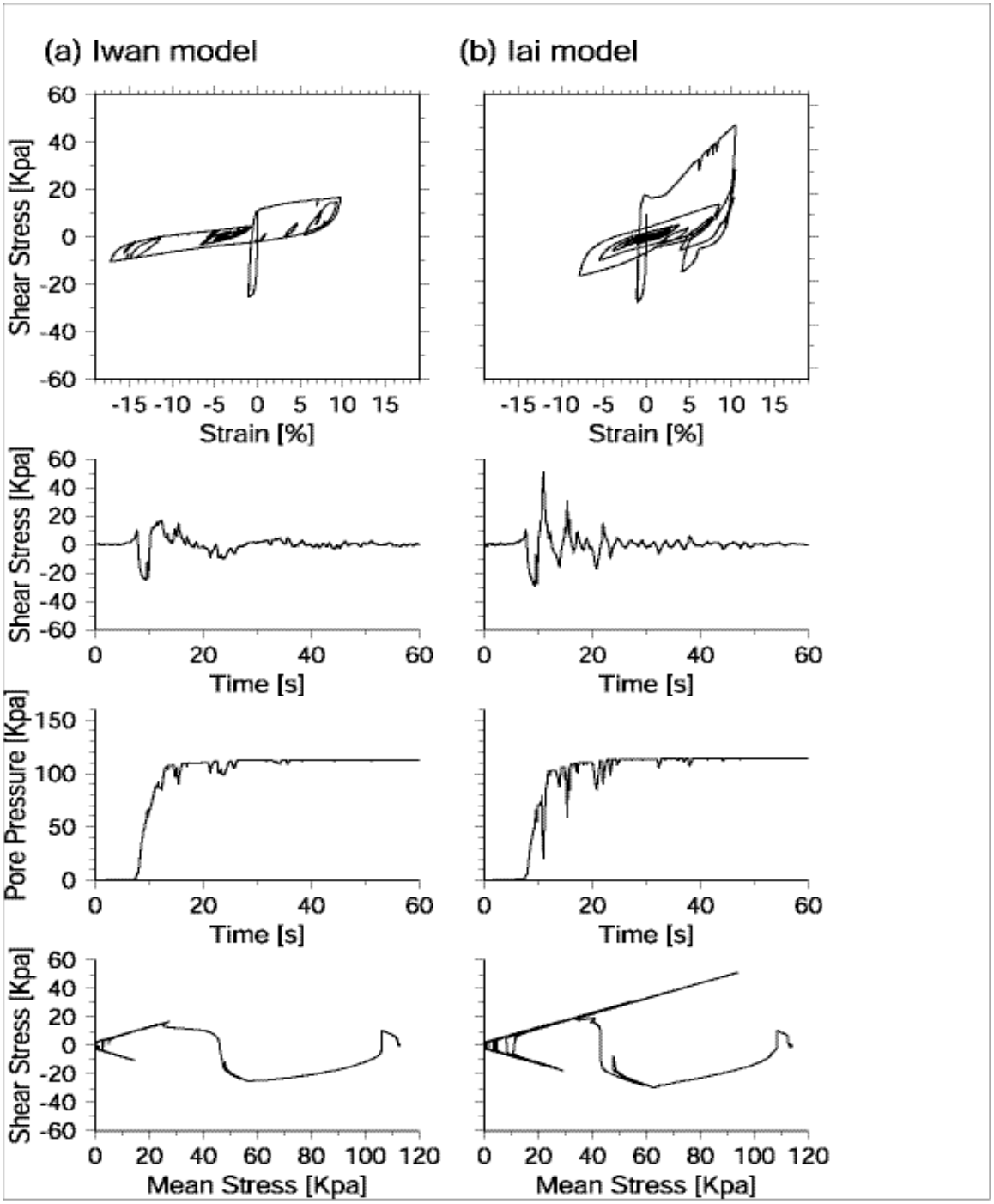

Figure 19: Calculated hysteresis loop, time histories of stress and pore pressure, and stress path at 20m depth (within the sand layer 10-27 m) for Iwan model (a) and Iai (b). The EW ground motion from the scenario earthquake is used as input.

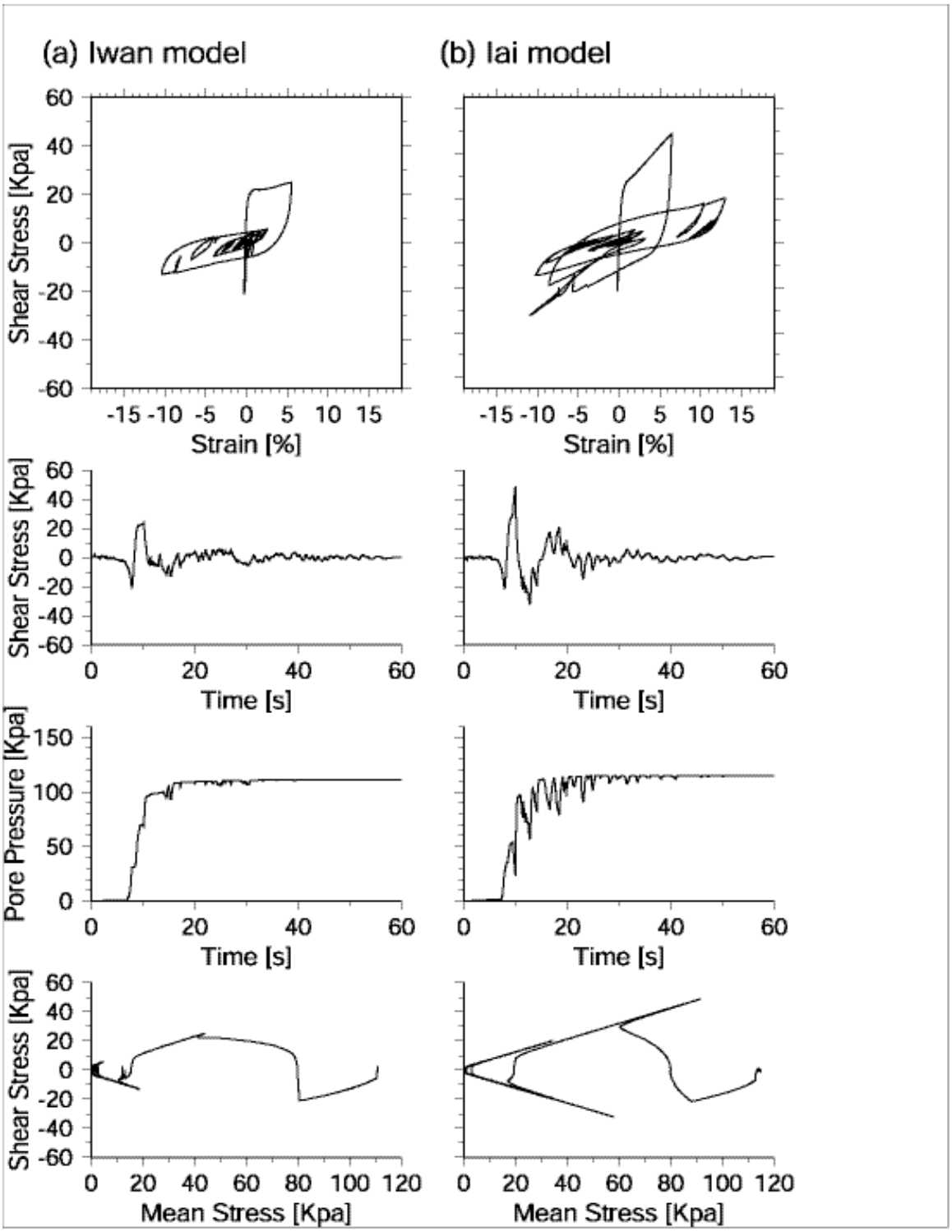

Figure 20: Calculated hysteresis loop, time histories of stress and pore pressure, and stress path at 20m depth (within the sand layer 10-27 m) for Iwan model (a) and Iai (b). The NS ground motion from the scenario earthquake is used as input.